# Micron-scale plasma membrane curvature is recognized by the septin cytoskeleton

Andrew A. Bridges,[1,2] Maximilian S. Jentzsch,[1] Patrick W. Oakes,[3] Patricia Occhipinti,[1] and Amy S. Gladfelter[1,2]

[1]Department of Biological Sciences, Dartmouth College, Hanover, NH 03755
[2]The Bell Center, Marine Biological Laboratory, Woods Hole, MA 02543
[3]Department of Physics, Institute for Biophysical Dynamics and James Franck Institute, University of Chicago, Chicago, IL 60637

Cells change shape in response to diverse environmental and developmental conditions, creating topologies with micron-scale features. Although individual proteins can sense nanometer-scale membrane curvature, it is unclear if a cell could also use nanometer-scale components to sense micron-scale contours, such as the cytokinetic furrow and base of neuronal branches. Septins are filament-forming proteins that serve as signaling platforms and are frequently associated with areas of the plasma membrane where there is micron-scale curvature, including the cytokinetic furrow and the base of cell protrusions. We report here that fungal and human septins are able to distinguish between different degrees of micron-scale curvature in cells. By preparing supported lipid bilayers on beads of different curvature, we reconstitute and measure the intrinsic septin curvature preference. We conclude that micron-scale curvature recognition is a fundamental property of the septin cytoskeleton that provides the cell with a mechanism to know its local shape.

## Introduction

Micron-scale plasma membrane curvature exists at the base of neuronal outgrowths, cilia, and the cytokinetic furrow. Although it is well known that proteins can sense and generate curvature on the nanometer scale (e.g., BAR domain proteins) via numerous mechanisms, it is unclear whether proteins can directly sense shape on the micron scale, which is the level of many cell shape features (Zimmerberg and Kozlov, 2006). Dynamic changes in cell shape are central to processes as diverse as blood clotting, neurogenesis, and cancer cell metastasis. Thus, we reasoned that cells may have a capacity to sense local cell shape and use this information to inform behavior.

Septins, which are conserved filament-forming, membrane-associated proteins, are found at regions of cells which are characterized by micron-scale curvature, including the cytokinetic furrow and the bases of cell branches in neurons, fungi, and ciliates (Fares et al., 1995; Helfer and Gladfelter, 2006; Tada et al., 2007; Xie et al., 2007; Hu et al., 2010). At these sites, septins tether organelles, restrict diffusion, rigidify the cell cortex, and spatially localize signaling (Longtine et al., 2000; Tooley et al., 2009; Gilden and Krummel, 2010; Hu et al., 2010; Gilden et al., 2012; Chao et al., 2014). Perturbation of septin genes results in abnormal cell morphology, cytokinesis defects, and inviability in many organisms (Gladfelter et al., 2005; Mostowy et al., 2011; Mostowy and Cossart, 2012). Humans possess 13 septins which are implicated in numerous pathologies, including neurodegenerative diseases, infertility, and cancers (Dolat et al., 2014). Despite their importance, little is understood about the molecular function of septins compared with other cytoskeletal proteins. Given their capacity to self-assemble into rod-shaped complexes that are tens of nanometers in length and filaments on the plasma membrane that are microns in length, we hypothesized that septins are capable of micron-scale curvature recognition (Sirajuddin et al., 2007; Bertin et al., 2008; Bridges et al., 2014).

## Results and discussion

### Septins enrich at sites of positive curvature in *Ashbya gossypii*

To assess the curvature dependence of septin localization, we used *Ashbya gossypii*, a filamentous fungus that has similar genome organization to *Saccharomyces cerevisiae* (Dietrich et al., 2004). During hyphal growth in *A. gossypii*, septins assemble into three genetically and spatially separable higher-order structures associated with the cell cortex: (1) straight, stable bundles or "bars" of filaments; (2) thin, dynamic filaments, often enriched at sites of cell growth; and (3) dense assemblies at the base of lateral branches, reminiscent of septin localization at the base of outgrowths in neurons (Fig. 1 A, Fig. S1 A, and Video 1; Helfer and Gladfelter, 2006; DeMay et al., 2009). *A. gossypii* branches emerge in a variety of orientations

Correspondence to Amy S. Gladfelter: amy.gladfelter@dartmouth.edu

Abbreviations used in this paper: PC, L-α-phosphatidylcholine; PI, L-α phosphatidylinositol; RCF, relative centrifugal force; RhPE, L-α-phosphatidylethanolamine-*N*-(lissamine rhodamine B sulfonyl); ROI, region of interest; SUV, small unilamellar vesicle; WT, wild type.



The Rockefeller University Press $30.00
J. Cell Biol. Vol. 213 No. 1 23–32
www.jcb.org/cgi/doi/10.1083/jcb.201512029

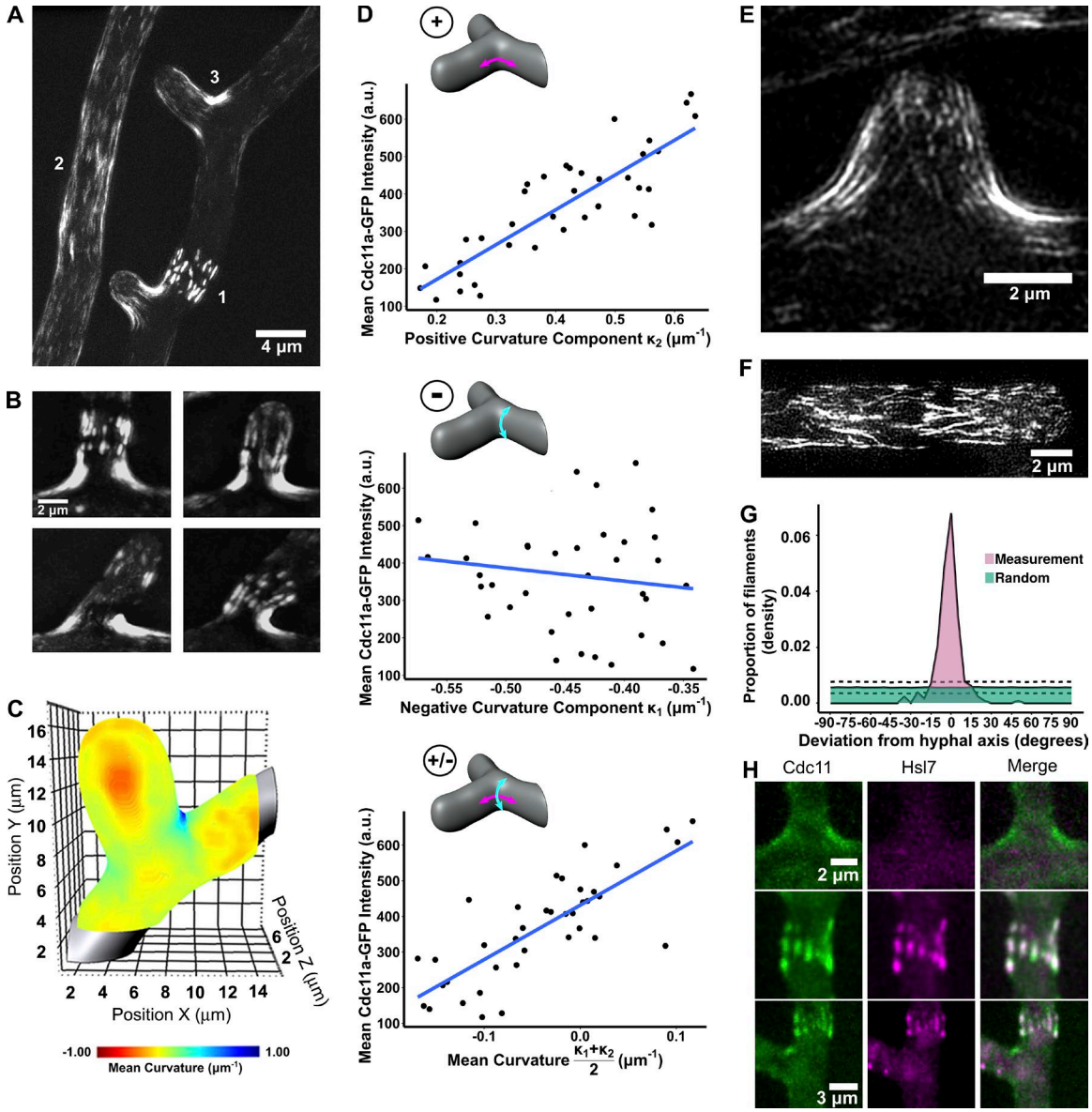


Figure 1. **Septin abundance scales with positive curvature in *A. gossypii*.** (A) Septin higher-order structures in *A. gossypii*, visualized by Cdc11a-GFP using structured illumination microscopy (SIM). Straight bundles (1), thin filaments (2,) and branch assemblies (3) exist in the same cell. (B) SIM images of Cdc11a-GFP signal at the base of four lateral branches emanating from hyphae at distinct angles, producing different curvatures. (C) Mean curvature heat map produced by imaging Blankophor in the *A. gossypii* cell wall followed by curvature analysis. For this display, curvature was mapped onto the external surface and values were inverted to represent curvature as viewed from the cell interior. (D) Cdc11a-GFP intensity at the base of branches plotted against positive and negative principal curvatures and mean curvature as viewed from the cell interior. Diagrams illustrate the curvature measured in each plot. (E) Filament orientation at the base of branches visualized by Cdc11a-GFP SIM. (F) Filament orientation in hyphae, away from sites containing a positive curvature component. (G) Filament orientation relative to the hyphal axis was measured compared with a random simulation of filament orientations (solid lines, mean; dotted line, SD; $n$ = 263 filaments in 13 hyphae). (H) Colocalization of Cdc11-mCherry (green) and Hsl7-GFP (magenta) at the base of branches and straight bundles in *A. gossypii*.

creating a situation where different curvatures are present locally at the base of the same branch. We found that the septin Cdc11a is asymmetrically localized and preferentially enriched on the side of a branch with the highest curvature, even though both surfaces have access to the same local soluble pool of septins (Fig. 1 B). This suggested that septins localize in a curvature-dependent manner.

To systematically determine the relationship between cell shape and septin localization, we visualized the cell outline using a cell wall dye and measured curvature proximal to *A. gossypii* branches (Fig. 1 C and Fig. S2, A–C). Considering that the bases of branches are saddle shaped, we analyzed septin localization versus the two orthogonal principal curvatures and mean curvature. For clarity, we report the measured curvature of the cytoplasmic face of the cell, which is what septins experience. From this perspective, *A. gossypii* are primarily composed of a negative principal curvature, which runs around the tube-shaped cells, including at the base of branches. In contrast, a positive principal curvature is only found at the base of branches, and it runs from the main hyphae into branches, where the membrane bends inward toward the cytoplasm (Fig. S2 A). We found a strong relationship between Cdc11a-GFP

enrichment and the positive curvature component (r = 0.850) and little correlation with the negative principal curvature (r = 0.145; Fig. 1 D). Consistent with a preference for positive curvature, septin abundance increased as the mean curvature increased and did not peak at zero, which is what would be expected with preference for the saddle point (r = 0.790; Fig. 1 D). Individual septin filaments were readily seen to align and add along the arc of branches, further supporting that septins are likely responding to positive curvature (Fig. 1 E, Fig. S1 B, and Video 1). Septins were also detected at locations of even higher positive membrane curvature in stressed cells or in yeast cells responding to mating pheromone, consistent with findings for mammalian cells responding to osmotic shock (Fig. S1, D–E; Gilden et al., 2012). In unbranched regions of the cell, septin filaments aligned parallel to the hyphal growth axis, avoiding the more negative curvature that would be encountered if filaments aligned orthogonal to the growth axis (Fig. 1, F and G; and Fig. S1 C). Thus, septins enrich at sites of positive curvature, and the degree of curvature corresponds to the abundance of septins recruited.

If septins do sense positive curvature, we predicted that septin-interacting proteins could be differentially recruited to distinct higher-order structures. Indeed, we found that Hsl7, a methyltransferase involved in regulating nuclear division, bound exclusively to straight septin bars but never to septins localized at branch sites ($n = 41$; Fig. 1 H; Helfer and Gladfelter, 2006). Collectively, these results suggest that eukaryotic cells possess a mechanism to recognize micron-scale curvature, and signaling proteins (e.g., Hsl7) can distinguish between curved and straight septin platforms. It is unclear from these experiments, however, if septins alone possess the ability to sense micron-scale curvature or if an upstream factor recognizes the local geometry and in turn recruits septins.

### Purified septins recognize micron-scale membrane curvature

To address if septins can directly differentiate among micron-scale curvatures, we set up a minimal system to measure septin adsorption on positively curved surfaces. We used recombinantly expressed and purified yeast septin complexes containing Cdc10, Cdc3, Cdc12, and Cdc11-SNAP and supported lipid bilayers containing anionic phospholipids formed on silica beads of different fixed curvatures (diameters, 0.3, 1.0, 3.0, 5.0, and 6.5 µm; Figs. 2 A and S3 A). Indeed, when we mixed septins with bilayer-coated beads, we found septin adsorption was dependent on bead diameter and thus the curvature of the bead (Fig. 2, A and B; and Video 2). At physiological concentrations, septins were maximally recruited to intermediately sized beads (1–3 µm), with little to no recruitment to both very large (5–6.5 µm) or very small beads (0.3 µm; Fig. 2 C; Bridges et al., 2014). These measurements reveal approximately eight times more septins bound to the 1.0-µm beads than the 6.5-µm beads at 100-nM septin complex concentration after normalizing for surface area using lipid dye intensity. The relative abundance of septin on each bead size was found to be highly septin concentration–dependent (Fig. 2, D and E). Notably, the preference for the intermediate-sized beads is similar to the curvatures in cells where septins are enriched ($\kappa = 0.6\ \mu m^{-1}$; Fig. 1 D). These results demonstrate that septins can readily distinguish between micron-scale curvatures in the absence of other cellular factors.

### Septin affinity for membranes varies depending on curvature

How do septins differentiate between membrane curvatures? We reasoned that either septins have a higher affinity for membranes of specific curvatures (such as found on 1–3-µm beads) or their maximum binding capacity ($B_{max}$—effectively how much septin can fit on a given curved surface) is greater on these curvatures. Because of limitations in protein yield, we were unable to measure saturation binding curves on all bead sizes. To circumvent this problem, we analyzed binding over time to 1- and 5-µm beads (Fig. 3 A). We found that septins accumulated faster on the smaller beads, suggesting that $B_{max}$ differences alone could not explain differences in adsorption. In our analysis of saturation binding to larger beads, we noticed another interesting feature. The intermediate binding of septins to 5-µm beads at high septin concentrations, produced by averaging many beads, was actually composed of a nearly bimodal distribution of septin adsorption (Fig. 3 B). A population of beads displayed nearly the same adsorption as the 1-µm beads, whereas others had almost no septin enrichment, suggesting that the adsorption process is highly cooperative. Because adsorption was found to be highly salt dependent, by lowering the salt conditions to well below physiological levels (50 mM KCl), we were able to achieve similar binding of septins to 1- and 5-µm beads (Figs. 3 C and S3 B). Collectively, these results suggest that an effective affinity difference rather than $B_{max}$ is the driving force behind septin curvature preference.

### Single septin complexes recognize curvature but must polymerize for stable membrane association

Next, we wondered whether septin curvature sensing required septin–lipid interaction at their predicted anionic lipid-binding module, a short polybasic region on the N terminus of each septin protein. To determine this, we used an alternative means to recruit septins using lipid mixtures containing $Ni^{2+}$-NTA modified headgroups and septin complexes containing an N-term 6xHIS tag on Cdc12. With this method, septin complexes still displayed a curvature preference for 1.0-µm beads, albeit slightly reduced compared with anionic lipids (1.4× enrichment on 1- over 3-µm beads compared with 3.7× enrichment on anionic mixtures at the same septin concentration; Fig. 4 A). This indicates that conformational changes induced by specific lipid interactions are not essential for curvature sensing but may tune it to a certain degree.

Given the micrometer scale of the curvatures detected by septins, we next asked whether complexes must polymerize to sense curvature. Alternatively, single septin complexes (32-nm-long rods) may have a higher affinity for curved membranes. To address this issue, we introduced mutations into the α6 helix of the Cdc11 N–C interface, which mediates polymerization of complexes into filaments (Sirajuddin et al., 2007). These mutant septins purified as complexes, yet failed to polymerize (Fig. 4 B and Fig. S3, C–E). When we recruited cdc11*α6* mutant complexes via the Cdc12 6xHIS tag and $Ni^{2+}$-NTA lipids, we found that the curvature preference was still intact (Fig. 4 C). Similarly, wild-type (WT) complexes at high salt concentrations that prevent polymerization and association with anionic membranes also retain curvature preference on $Ni^{2+}$-NTA–containing bilayers (Fig. 4 D; Booth et al., 2015). These results indicate that individual septin complexes are able to perceive micron-scale curvature differences.

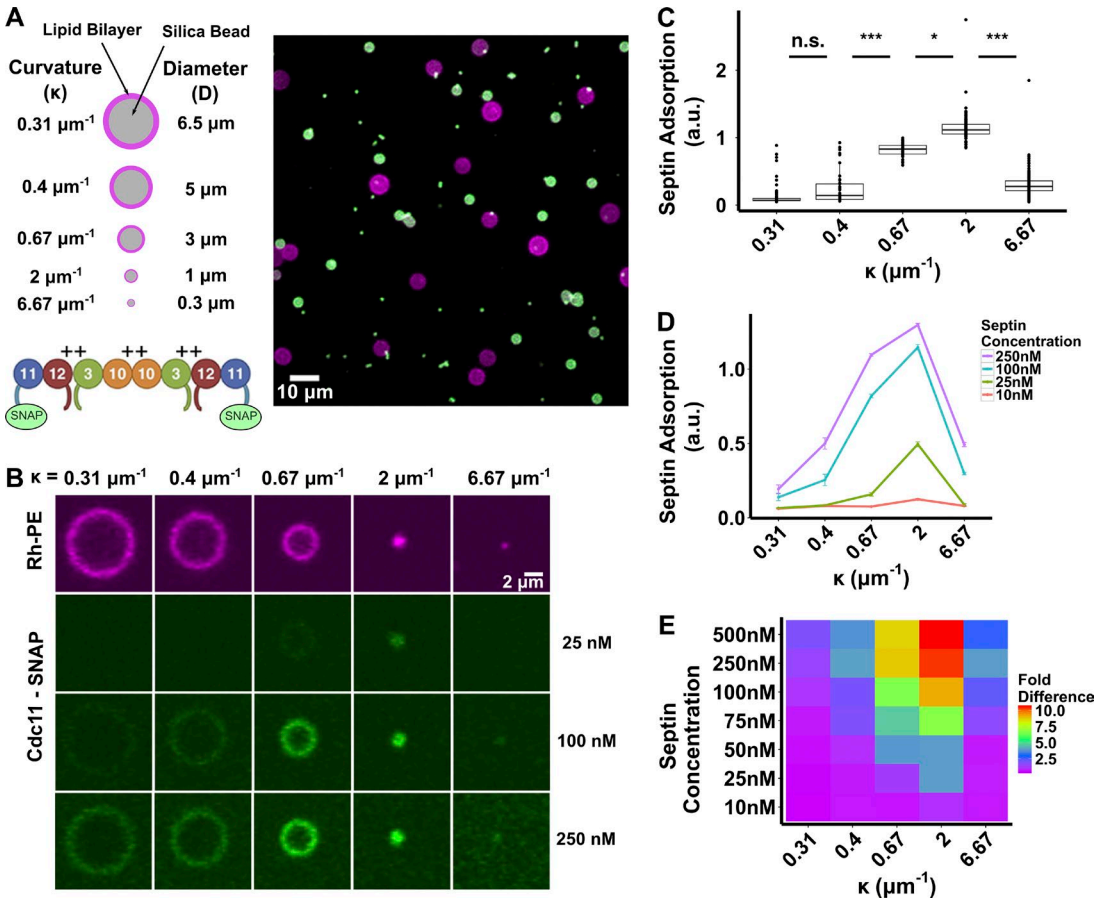


Figure 2. **Septins recognize micron-scale positive membrane curvature.** (A) Supported lipid bilayer (25% PI and 75% PC) and trace Rh-PE–coated silica beads ranging from 0.3 to 6.5 µm in diameter mixed with 50 nM *S. cerevisiae* septin complex containing Cdc11-SNAP488 for visualization. The Rh-PE is shown in magenta, and Cdc11-SNAP488 is shown in green. (B) Mean intensity images of 10 beads for each condition. (C) Septin adsorption to each bead size at 100-nM septin complex. (D) Septin adsorption to beads as a function of concentration. (E) Heat map of fold difference in septin adsorption to beads as a function of concentration. Data were normalized to the lowest detectable septin adsorption, on 1-µm beads at 10-nM septin complex concentration. 500 nM was the highest experimentally attainable septin complex concentration that could be mixed with beads. In C–E, $n \geq 32$ for each size, and error bars represent standard error. Dunn test results: ***, $P < 0.005$; *, $P < 0.05$. n.s., not significant.

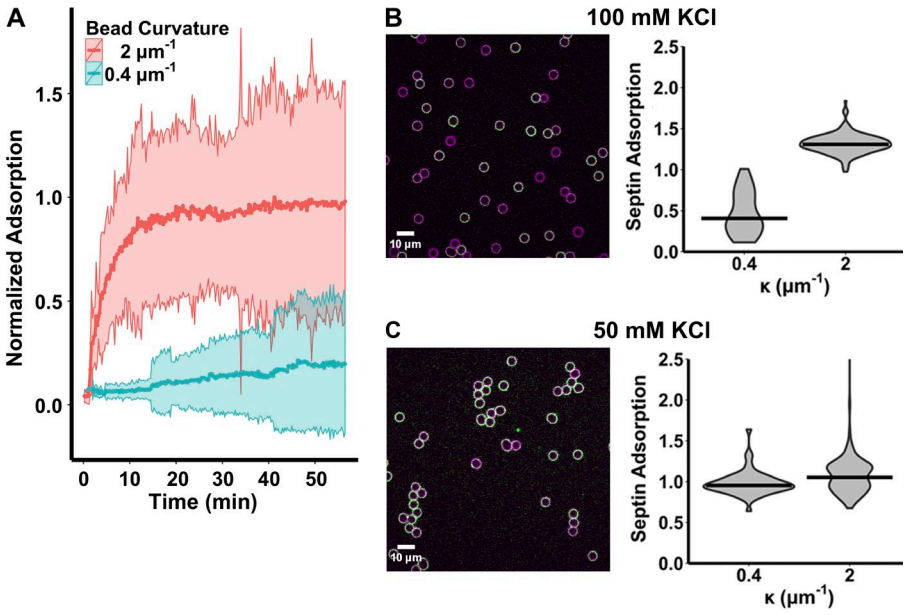


Figure 3. **Septin affinity for membranes varies depending on curvature.** (A) Adsorption of septins to silica beads over time on 1 µm ($\kappa = 2\ \mu m^{-1}$) and 5 µm ($\kappa = 0.4\ \mu m^{-1}$) at 250-nM septin complex concentration. Solid lines represent means, and shaded areas represent SD (average n/time point: $2\ \mu m^{-1}$ = 158 beads and $0.4\ \mu m^{-1}$ = 18 beads). (B) Adsorption of 500-nM septin complexes on 1-µm ($\kappa = 2\ \mu m^{-1}$) and 5-µm ($\kappa = 0.4\ \mu m^{-1}$) beads in 100 mM KCl. (C) Adsorption of 500-nM septin complexes on 1-µm ($\kappa = 2\ \mu m^{-1}$) and 5-µm ($\kappa = 0.4\ \mu m^{-1}$) bilayer-coated beads in 50 mM KCl. In B and C, $n \geq 50$ for each size; black bars represent medians.

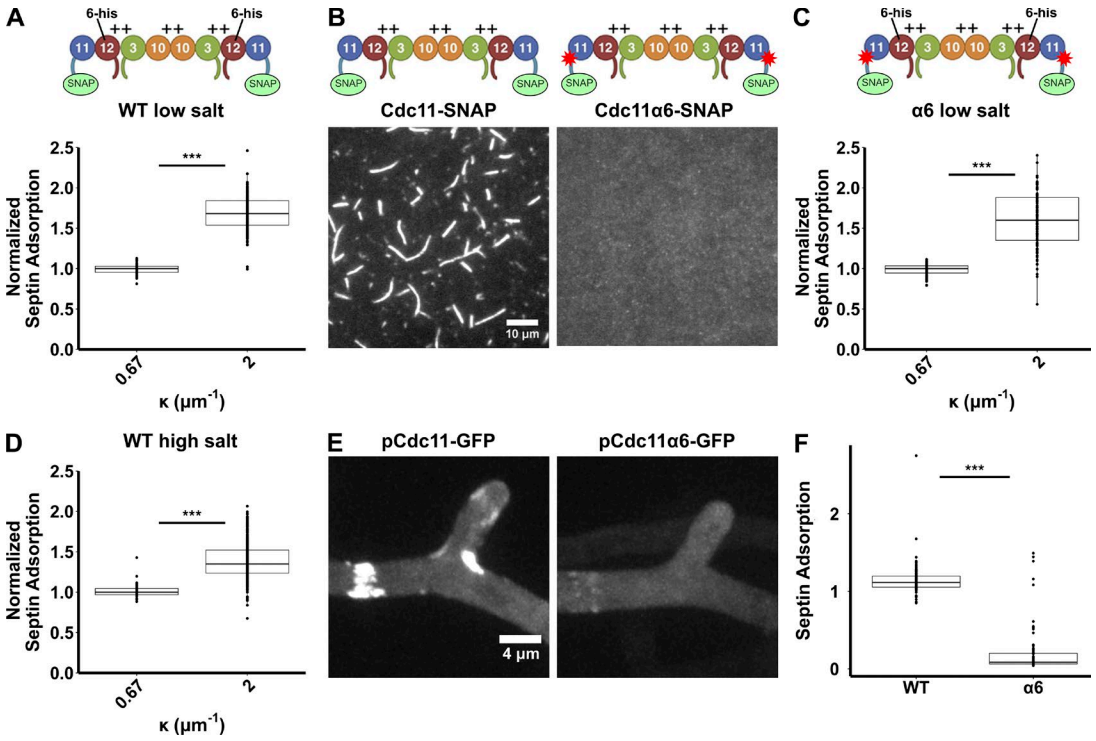


Figure 4. **Curvature preference remains intact in single complexes, but filament formation is required for stable membrane association.** (A) Adsorption of 25 nM 6xHIS WT Cdc11–SNAP488 complexes to 1-μm (κ = 2 μm$^{-1}$) and 3-μm (κ = 0.67 μm$^{-1}$) beads coated in 2% DGS-Ni$^{2+}$ NTA lipids in 100 mM KCl. For visualization of fold enrichment, data were normalized to 3-μm beads. (B) WT Cdc11–SNAP complexes and Cdc11-α6–SNAP complexes, containing point mutations in the polymerization interface of Cdc11, were diluted to 250 nM in 50 mM KCl to promote filament formation and visualized on a polyethylene glycol–coated coverslip. (C) Adsorption of 100 nM 6xHIS Cdc11-α6–SNAP488 complexes to 1-μm (κ = 2 μm$^{-1}$) and 3-μm (κ = 0.67 μm$^{-1}$) beads coated in 2% DGS-Ni$^{2+}$ NTA lipids in 100 mM KCl. (D) Adsorption of 25 nM 6xHIS WT Cdc11–SNAP488 complexes to 1-μm (κ = 2 μm$^{-1}$) and 3-μm (κ = 0.67 μm$^{-1}$) beads coated in 2% DGS-Ni$^{2+}$ NTA lipids in 300 mM KCl. (E) WT and α6 mutant Cdc11-GFP expressed and imaged in live *A. gossypii*. (F) Membrane adsorption of 100 nM WT and Cdc11-α6–SNAP488 complexes on anionic-supported lipid bilayer (25% PC, 75% PI, and trace RhPE)–coated 1-μm beads. In A, C, D, and F, $n \geq 43$ for each size. Dunn test results: ***, $P < 0.005$.

We then assessed what happens when a nonpolymerizable septin is expressed in cells. When cdc11*α6* was expressed in *A. gossypii* cells, we found no incorporation of cdc11*α6*-GFP into septins at the base of branches but could detect very faint association in the form of puncta with straight septin bundles (Fig. 4 E). Consistent with this result, when we mixed these cdc11*α6* mutant complexes with 1.0-μm beads coated with L-α-phosphatidylcholine (PC)/L-α phosphatidylinositol (PI) bilayers, we found that adsorption to bilayers was dramatically reduced compared with WT septin complexes (Fig. 4 F). This result implies that avidity through polymerization permits stable septin association with anionic lipids. In addition, this could mean that septins in the straight bundles are recruited to the cell cortex by other proteins or have lateral interactions that are capable of recruiting nonpolymerizing septin complexes. Collectively, these data suggest that the septin complex has an intrinsic curvature preference; however, for stable association with membranes to occur, septins must polymerize, indicating that polymerization is critical for retention of septin complexes at sites of curvature in cells. In addition, a small difference in complex affinity for curved membranes could be amplified by a cooperative adsorption process.

## Septin curvature recognition is conserved beyond the fungal kingdom

Finally, we sought to determine whether septin curvature recognition is conserved beyond the fungal kingdom. Previous work has shown that human septin complexes form rings when polymerized in vitro and in the absence of F-actin in mammalian cells and are able to tubulate giant unilamellar vesicles, which we hypothesized were a manifestation of the same properties that could drive curvature sensing (Kinoshita et al., 2002; Tanaka-Takiguchi et al., 2009). Similar to fungal systems, many distinct septin structures can exist during interphase (Kinoshita et al., 2002; Gilden and Krummel, 2010; Bowen et al., 2011; Bridges and Gladfelter, 2015). These include straight perinuclear filaments, regions of colocalization with the actin cortex, and at the base of cell protrusions in NIH-3T3 fibroblasts (Fig. 5 A). In an attempt to disentangle these structures, we perturbed the actin cytoskeleton and found septin abundance appeared to scale with the degree of membrane curvature (Fig. 5 B). To verify that mammalian septins also intrinsically possess the ability to distinguish between curvatures and to measure mammalian septin curvature preference, we purified complexes containing human SEPT2, SEPT6, and SEPT7 and added them to the anionic lipid bead-binding assay (Figs. 5 C and S3 G). Consistent with our observations with the fungal complexes, we found preferential adsorption on 1-μm beads (Fig. 5, C and D). This suggests that a fundamental property of the septins from widely divergent species is to recognize plasma membrane shape on the scale of microns, which has not been reported previously for other plasma membrane–binding proteins.

## Conclusion

What is the structural basis for micron-scale curvature recognition? One possibility is that septin complexes are curved and

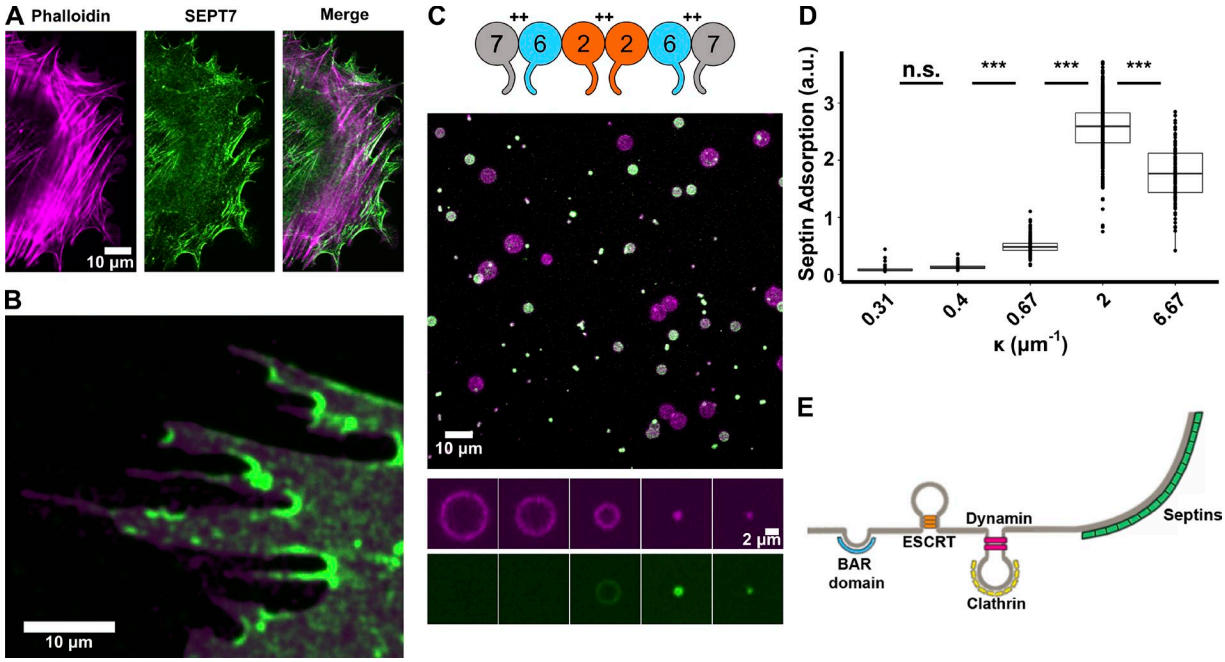


Figure 5. **Mammalian septins recognize membrane curvature.** (A) Phalloidin (magenta) and SEPT7 (green) localization, visualized by α-SEPT7 immunofluorescence, in NIH 3T3 fibroblasts. (B) SEPT7 localization (green) in NIH 3T3 fibroblasts treated with 1 µM latrunculin A for 15 min to disrupt actin-dependent septin localization. The cell outline (magenta), was produced by imaging Alexa Fluor 647–conjugated wheat germ agglutinin. (C) 50 nM human septin complexes (SEPT2–SEPT6–SEPT7) labeled with NHS-Alexa Fluor 488 on supported lipid bilayer–coated silica beads. (D) Adsorption of 50 nM human septin complex on bilayer-coated beads (25% PC, 75% PI, and trace RhPE). $n \geq 67$ for each size. Dunn test results: ***, $P < 0.005$; n.s., >0.05. (E) Model displaying the scale of septin curvature sensing compared with other established proteins that interact with curved membranes.

as such preferentially associate with curved membranes (Fig. S3 H; Bertin et al., 2008). Alternatively, the human complex may dynamically hinge in the center (Fig. S3 I; Sirajuddin et al., 2007). In either case we propose that one of two principles drives septin curvature recognition: either the septin–lipid interaction is geometrically favorable when membranes are curved or interacting with a curved membrane promotes an energetically favorable septin complex conformation. Given that humans have 13 septin genes, it is likely that alternative septin complexes, containing different septin proteins, could tune and regulate curvature sensing. From the data presented in this work, we cannot rule out that on anionic phospholipid membranes, curvature promotes septin adsorption via additional mechanisms other than the affinity of single septin complexes. Given the importance of polymerization for membrane adsorption demonstrated in this work, it is also possible that curved membranes promote polymerization and thereby membrane affinity. Alternatively, stochastic fragmentation or depolymerization of filaments could be reduced on curved membranes.

This work identifies the first direct sensor of micron-scale curvature in eukaryotic cells and demonstrates that septin complexes have an intrinsic capacity to recognize specific curvatures (Fig. 5 E). Although a bacterial protein has been shown to recognize the micron-scale forespore membrane, and myosin-II has been shown to enrich in areas of low curvature, in neither case is it clear how the nanometer to micron scales are linked (Ramamurthi et al., 2009; Elliott et al., 2015). The elongated rod-shaped complexes make septins sufficiently long to perceive micron-scale differences in shape before polymerization; however, polymerization must take place for stable membrane association. Interestingly, septin complexes can make curved bundles of F-actin; however, it is unclear that this is related mechanistically or functionally to the work reported here (Mavrakis et al., 2014). Although we acknowledge that the same curvature sensing properties of septins could also produce membrane curvature, we hypothesize that the forces required to deform membranes on the micron scale in a cell, particularly in fungi which have a rigid cell wall, are too great for septins alone to carry out. We propose that septins at the base cell protrusions may serve as landmarks and signaling platforms so the cell can know its local shape long after such topologies have been constructed.

## Materials and methods

### *A. gossypii* growth and imaging

*A. gossypii* cultures were grown for 15–17 h in *A. gossypii* full media at 30°C. Cells were collected by gentle centrifugation, resuspended in *A. gossypii* low fluorescence media, and mounted between a 1.5 coverslip and a 0.5–1.5% agar pad hydrated with low fluorescence media. Before imaging, cells were grown 22°C on the agar pad for 1 h.

Display images (Fig. 1, A and B; and Fig. S1, A, D, and E) were acquired on a Nikon N-SIM microscope using a 100× Plan Apo 1.49 NA oil lens with 14 bits per pixel on an iXon Ultra DU-897 camera (Andor Technology) with EM gain; laser power and exposure were adjusted to keep pixel intensities in the first quarter of the camera dynamic range. Z-stacks were acquired with 0.125-µm-thick z-sections and 15 images per optical slice (three angles and five phases). 3D reconstruction was performed in Elements software (version 40.30.01; Nikon). Reconstruction parameters were chosen to match best septin localization observed on traditional wide-field microscopes while maximizing resolution.

For analysis of curvature at the base of *A. gossypii* branches, the cell wall was localized using Blankophor (MP Biomedicals), whereas

septins were imaged using Cdc11a-GFP replaced at the endogenous locus (AG384). Z-stacks of both channels were imaged with a step size of 0.2 µm on a Nikon A1RSi laser scanning confocal microscope using a 100× Plan Apo 1.49 NA oil lens. Blankophor was excited with a 407-nm laser, and GFP was excited with a 488-nm laser with the pinhole open to 2 AU. See the following section for a description of the curvature analysis.

For imaging Cdc11a-GFP filament orientation (Fig. 1, E and F; and Fig. S1 C), super-resolution 3D-SIM images were acquired on a DeltaVision OMX V4 (GE Healthcare) equipped with a 60×/1.42 NA PlanApo oil immersion objective (Olympus), 405-, 488-, 568- and 642-nm solid-state lasers (100 mW) and sCMOS cameras (pco.edge). Z-stacks were acquired with 0.125-µm-thick z-sections and 15 images per optical slice (three angles and five phases). Images were reconstructed using Wiener filter settings of 0.005, and optical transfer functions were measured specifically for each channel with SoftWoRx 6.1.3 (GE Healthcare) to obtain super-resolution images with a twofold increase in resolution both axially and laterally. Unless otherwise stated, cells were imaged at 22°C.

### *A. gossypii* curvature analysis

Z-stacks of septins in *A. gossypii* branches were analyzed using Imaris 7.7.2 (Bitplane AG). For curvature analysis in 3D, images were resampled using the Imaris "Resample 3D" command to produce voxels of isotropic dimensions. Images were subsequently background subtracted using the software's Gaussian filter for background determination (width 10.6 µm) and then cropped to eliminate all but the curved region on one side of any given branch. Individual surfaces were created for the Cdc11a-GFP signal and the Blankophor signal. The GFP surface was then used to determine the mean GFP intensity. It also served as a guide for the placement of the region of interest (ROI) for curvature measurements, which was performed on the surface created from the Blankophor signal. Curvature analysis was conducted on the cytoplasmic face of the Blankophor surface, as this is the side to which septins associate. The ROI used for curvature analysis was the area of intersection between the Blankophor surface and the GFP surface (Fig. S2 C). The final ROI includes a slightly larger area than the surface intersection, thereby including more points in the curvature calculation than desired. However, these unwanted points only represented a negligible percentage of the total number of points used for the curvature calculation (~4.5% in Fig. S2 C), thereby not having a substantial effect on the curvature calculation. Using custom curvature analysis Imaris XTensions written in MATLAB R2015a (MathWorks), the following curvature values were calculated within the ROI: mean curvature, Gaussian curvature, and both principal curvatures. The core of the custom curvature analysis XTension was created by Matthew J. Gastinger (Bitplane). This XTension uses Dirk-Jan Kroon's "Patch Normals" and "Patch Curvature" functions (Kroon, 2009, 2014). Curvature values, as well as the mean Cdc11a-GFP intensity, were exported into Microsoft Excel files. Files were then imported into R version 3.2.2 using RStudio 0.99.467 (R Foundation for Statistical Computing), where all of the statistical analyses took place. Plots were generated using the ggplot2 package in R (Wickham, 2009).

### Analysis of hyphal filament orientation

To evaluate whether filaments within hyphae were aligned to minimize negative curvature, filament orientation was compared with the hyphal growth axis. This analysis focused on one straight segment of a single hypha at a time to avoid areas where hyphal bending occurred. To determine the hyphal orientation, the cell outline was traced using Fiji (version 1.50b; National Institutes of Health), and the arithmetic mean of both sides of the hypha served as the orientation relative to the horizontal axis. Angle measurements were always performed in the direction of cell growth using the "Measure_Angle_and_Length" macro available at http://rsb.info.nih.gov/ij/macros/.

Within the cell outline, filament angles with respect to horizontal were measured. Using a custom MATLAB script, the filament orientation with respect to hyphal orientation was calculated. A total of 263 filament angles were measured. The distribution of these measurements was then compared with a random distribution. To obtain the random distribution, 263 angles between –90 and 90° were chosen randomly from a uniform distribution using R's *runif* function. This process was repeated 1,000 times, which allowed for the calculation of mean and SD density values. The measurement and random values were compiled and plotted in R (Wickham, 2007; Winston, 2014).

### Yeast septin purification and labeling

BL21 (DE3) *Escherichia coli* cells were transformed with a duet septin expression platform (see Generation of strains section), selected for with ampicillin and chloramphenicol, and induced to express with 1 mM IPTG at an $OD_{600}$ of 0.6–0.7. After 24 h of growth at 22°C, cells were harvested by centrifugation at 10,000 relative centrifugal force (RCF) for 5 min. Pellets were either lysed immediately or stored at –80°C until lysis. Cells were thawed and incubated in lysis buffer (50 mM $KH_2PO_4$, pH 8.0, 1 M KCl, 1 mM $MgCl_2$, 1% Tween-20, 10% glycerol, 1× protease inhibitor [Roche], and 20 mM imidazole), with 1 mg/ml lysozyme for 30 min on ice. Cells were then sonicated for 20 s, and resulting whole-cell extract was clarified by centrifugation at 4°C for 30 min at 20,000 rpm in an SS-34 rotor in a Sorvall RC-6 centrifuge. Clarified supernatant was placed on an equilibrated $Ni^{2+}$-NTA agarose (QIAGEN) column containing 2 ml of resin per liter of *E. coli* culture. Bound protein was washed three times (5× column volume) with wash buffer (50 mM $KH_2PO_4$, pH 8.0, 1 M KCl, and 20 mM imidazole) and eluted with a high imidazole concentration (50 mM $KH_2PO_4$, pH 8.0, 300 mM KCl, and 500 mM imidazole). Protein was dialyzed into septin storage buffer (50 mM Tris, pH 8.0, 300 mM KCl, 1 mM DTT) to remove excess imidazole overnight via two 500-ml steps using 10,000 MW cutoff cassettes (Thermo Fisher Scientific). Subsequently, the 6xHIS tag on Cdc12 was removed by treatment with ProTEV Plus protease (Promega). Protein was then run over a second $Ni^{2+}$-NTA column to remove cleaved 6xHIS tag, the TEV protease, and $Ni^{2+}$-NTA binding contaminants. SNAP Surface 488 (New England Biolabs) was incubated with protein eluate at a 1.5× excess molar ratio at 4°C overnight. Excess dye was removed by dialysis with septin storage buffer. Purity was assessed by 10% SDS-PAGE, and protein concentration was determined by Bradford assay.

### Human septin purification

Human septin plasmids were a gift from M. Mavrakis (Institut de Biologie du Développement de Marseille, Marseille, France), and proteins were purified as described in Mavrakis et al. (2014). In brief, Bl21-(DE3) containing a plasmid encoding $His_6$-hSEPT2 and hSEPT6, and a second plasmid encoding h-SEPT7-Strep, were grown to an $OD_{600}$ of 2–3 and induced to express by 1 mM IPTG for 1 h. Cells were collected by centrifugation at 10,000 RCF for 5 min. Pellets were either lysed immediately or stored at –80°C until lysis. Cells were thawed and incubated in lysis/wash buffer (50 mM Tris, pH 8.0, 500 mM KCl, 5 mM $MgCl_2$, 1× protease inhibitor, and 10 mM imidazole), with 1 mg/ml lysozyme for 30 min on ice. Cells were then sonicated for 20 s, and resulting whole-cell extract was clarified by centrifugation at 4°C for 30 min at 20,000 rpm in a SS-34 rotor in a Sorvall RC-6 centrifuge. Clarified supernatant was placed on an equilibrated $Ni^{2+}$-NTA agarose (QIAGEN) column containing 2 ml of resin per liter of *E. coli* culture. Bound protein was washed three times (5× column volume) and eluted

with a high imidazole concentration (50 mM Tris, pH 8.0, 500 mM KCl, 5 mM $MgCl_2$, and 250 mM imidazole). Eluate was then immediately passed over a Strep-Tactin (IBA) sepharose column, and bound protein was washed three times (5× column volume; 50 mM Tris, pH 8.0, 300 mM KCl, and 5mM $MgCl_2$) and eluted with buffer containing desthiobiotin (50 mM Tris, pH 8.0, 300 mM KCl, 5 mM $MgCl_2$, and 2.5 mM desthiobiotin). Purity was assessed by 10% SDS-PAGE, and protein concentration was determined by Bradford assay.

For labeling of human complexes, septins were exchanged into a lower pH buffer (potassium phosphate, pH 6.5, 300 mM KCl, and 5 mM $MgCl_2$) and reacted with Alexa Fluor 488 NHS Ester to ensure labeling at the N terminus. Buffer was then exchanged by dialysis to remove excess dye, and septins were stored in 50 mM Tris, pH 8.0, 300 mM KCl, and 5 mM $MgCl_2$.

### Preparation of and experimentation with supported lipid bilayer microspheres

Septin lipid binding was evaluated using a lipid composition of 75 mol% PC (egg, chicken; 840051; Avanti Polar Lipids), 25% PI (liver, bovine; sodium salt; 840042; Avanti Polar Lipids), and >0.1% L-α-phosphatidylethanolamine-*N*-(lissamine rhodamine B sulfonyl) (Rh-PE; ammonium salt; egg-transphosphatidylated, chicken; 810146; Avanti Polar Lipids). Lipids were mixed in chloroform solvent, dried by a stream of argon gas, followed by at least 2 h in a vacuum. Lipids were hydrated for 30 min at 37°C at a final lipid concentration of 5 mM in buffer (20 mM Tris, pH 8.0, 300 mM KCl, and 1 mM $MgCl_2$) and bath sonicated (1510; Branson) to clarity (∼5 min) to form small unilamellar vesicles (SUVs).

To recruit septins via the 6xHIS tag on the N terminus of Cdc12, a lipid composition of 98 mol% 1,2-dioleoyl-*sn*-glycero-3-phosphocholine (850375; Avanti Polar Lipids) and 2 mol% 1,2-di-(9Z-octadecenoyl)-*sn*-glycero-3-[(N-(5-amino-1-carboxypentyl)iminodiacetic acid)succinyl] (nickel salt; 790404; Avanti Polar Lipids) was mixed in chloroform solvent, dried by a stream of argon gas followed by at least 2 h in a vacuum. Lipids were hydrated at 5 mM in filtered PBS at 37°C for 30 min and freeze-thawed in liquid nitrogen 30 times. Subsequently vesicles were bath sonicated to clarity (∼2 min).

SUVs were adsorbed onto nonfunctionalized silica microspheres (0.31, 0.96, 3.17, 5.06, and 6.46 µm mean diameter, rounded in text for simplicity; Bangs Laboratories) by mixing 50 nmol lipids with 440 $mm^2$ of silica microsphere surface area in a final volume of 80 µl for 1 h in a roller drum at 22°C (PC/PI mixtures) or 37°C (Ni-NTA/PC mixtures). Excess SUVs were removed by pelleting coated beads for 30 s at the minimum force required to pellet each bead size (see http://www.bangslabs.com/ for sedimentation properties) followed by 4× washes with excess buffer (100 mM KCl and 50 mM Tris, pH 8.0).

To measure binding of septins to supported lipid bilayer-covered microspheres, 25 µl of septins in septin storage buffer were added to 75 µl of a bead-buffer solution yielding a final buffer composition containing 5 $mm^2$ total lipid-bead surface area (100 mM KCl, 50 mM Tris, pH 8.0, 0.1% methylcellulose, 0.1% BSA [fatty-acid free; Sigma-Aldrich], and 1 mM DTT, unless otherwise stated). For human septin experiments, the buffer was 50 mM KCl, 50 mM Tris, pH 8.0, 0.1% methylcellulose, 0.1% BSA, 500 µM $MgCl_2$, and 1 mM DTT. Experiments comparing septin adsorption to multiple bead sizes were performed both in complex mixtures, containing multiple bead sizes, and in conditions where only one bead size was present. Because results were qualitatively similar, and for convenience in quantification (beads often attached to one another), data represented in graphs were acquired using mixtures of septins with individual bead sizes at a time. Plastic chambers were glued to polyethylene glycol–passivated coverslips, and the septin-microsphere mixture was incubated for at least 1 h at RT until equilibrium was reached. Beads were imaged on a laser scanning confocal microscope (A1RSi; Nikon) using a 100× Plan Apo 1.49 NA oil lens, with the pinhole open to 2.0 AU. The entire z-series were acquired using Elements software controlling a piezo z-drive (Mad City Labs) with Nyquist sampling for both rhodamine and 488 channels.

For analysis of septin binding, raw images were exported to Imaris 8.1.2 (Bitplane AG). Every image was individually background subtracted in both channels using the software's Gaussian filter for background determination (width, 31.4 µm). The surface of each bead was defined in a given field using the lipid channel, and beads that stuck together were excluded from analysis. From the surface of each bead, a sum rhodamine lipid intensity and sum septin intensity (SNAP–Surface488 for yeast complexes and Alexa Fluor 488 for human complexes) were exported into Microsoft Excel. Files were then imported into R version 3.2.2 using RStudio 0.99.467, where all further analyses took place. "Septin adsorption" was calculated by dividing the sum septin intensity by the sum rhodamine lipid intensity to control for any potential optical differences between bead sizes. Plots were generated using the ggplot2 package in R (Wickham, 2007; Winston, 2014). Statistical analyses were done on a plot by plot basis. In every case, a Levene test showed that equal variances could not be assumed across groups (Fox and Weisberg, 2011). This called for a nonparametric approach. Thus, a Kruskal-Wallis rank sum test was performed, followed by a Bonferroni-adjusted Dunn test (Wickham, 2007; Lisovich and Day, 2014; Dinno, 2015; Wickham and Francois, 2015; Warnes et al., 2015a,b). For each experimental condition (unique combinations of lipid composition, bead size, salt concentration, and septin concentration), the number of beads analyzed ranged from 32 to 743. Although SNAP-tagged Cdc11 was used for publication materials, qualitatively similar results were obtained with septin constructs containing Cdc11-GFP.

### Generation of strains

A complete table of strains used in this study can be found in Table S1. Plasmids are listed in Table S2 and oligos are listed in Table S3. To generate SNAP-labeled Cdc11 for recombinant expression in the septin complex (AGB501), pACYC-Duet with ScCdc3 and ScCdc11, (AGB400.1; gift from J. Thorner, University of California, Berkeley, Berkeley, CA), was cut with EcoRV-HF/KpnI-HF. The digest was subsequently cleaned over a PCR purification column (QIAGEN) and then treated with rAPid Alkaline Phosphatase (Roche). AGB493 (pRS416 ScCdc11-yeSNAPf) was then cut with EcoRV-HF/KpnI-HF and cleaned over a PCR purification column before ligating. Ligation was preformed of prepared vector and insert using NEB T4 DNA ligase followed by transformation into NEB 5α competent cells selected on plates of LB media with 34 µg/ml Alfa Aesar chloramphenicol. Individual colonies were mini-prepared using a QIAprep Spin Miniprep kit (QIAGEN). Verification digestion was performed with BamHI-HF.

To generate a cleavable 6xHIS-tagged Cdc12 for recombinant expression in septin complexes (AGB710), a Tobacco Etch Virus (TEV) site was added between 6xHIS and ScCDC12 in AGB401 (pET-Duet-6xHIS-ScCdc12/ScCdc10) using PCR with AGO1557/AGO1558 and PfuUltraII Fusion HS DNA polymerase (Agilent Technologies). The resulting PCR product was treated with DpnI and cleaned with a PCR purification kit. DNA was then transformed into NEB 5 α high-efficiency competent cells. Single colonies were then mini prepared with a mini spin kit (QIAGEN) and then sequenced through the TEV insertion with AGO172 and AGO1192.

To introduce E289R, Y291A, and R292E point mutations in the α6 helix of the NC interface of Cdc11 for recombinant expression (AGB744) in septin complexes, pACYC-Duet with ScCdc3 and ScCdc11-SNAP (AGB501) was mutated using PCR with AGO1613/AGO1614 and PfuUltraII Fusion HS DNA polymerase (Agilent

Technologies). The resulting PCR product was treated with DpnI and cleaned with a PCR purification kit. DNA was then transformed into NEB 5 α high-efficiency competent cells. Single colonies were then mini prepared with a mini spin kit and then sequenced through the point mutations with AGO1609 and AGO1251.

To create an analogous, nonpolymerizing cdc11α6 mutant for expression in *A. gossypii* (AGB849), a gBLOCK (IDT) of cdc11A from 3,861–4,560 (700 bp) was synthesized. This fragment contained mutations in homologous residues (in *A. gossypii* Cdc11a: E288R, Y290A, and R291E) and the restriction enzyme sites AflI–MluI for downstream cloning. PCR was performed on the fragment with AGO1770 and AGO1771. This fragment, and AGB214 (pRS416-Ag-CDC11A-GFP-GEN), were cut with AflII–MluI, and the vector was treated with rAPid Alkaline Phosphatase. Ligation was performed, and the product was verified by test digestion and sequencing with AGO130 and AGO1771. The plasmid was then introduced into *A. gossypii* by electroporation and selection was performed using G418.

### Septin pelleting assay and FCS

A sedimentation assay was performed to determine the polymerization state of septins by diluting septin complexes into a low salt buffer (50 mM KCl, 50 mM Tris, pH 8.0, and 1 mM DTT) for 2 h. Next, samples were centrifuged for 20 min at 22°C under 100,000 RCF (Optima Ultracentrifuge; Beckman Coulter). Supernatant was removed, and pellets were resuspended in the same volume. Samples were then analyzed by SDS-PAGE.

The FCS autocorrelation curve of fluorescent septin complexes in high salt buffer (300 mM KCl, 50 mM Tris, pH 8.0, and 1 mM DTT) was generated using commercial PicoQuant hardware and software on a Nikon A1 LSM, using a Plan Apo IR 60× WI 1.27NA objective. Identical laser intensity was used when comparing complexes containing Cdc11–SNAP–Atto488 and the mutant Cdc11-α6–SNAP–Atto488. Fluctuations in fluorescence intensity were monitored for 20 s for each experiment. The autocorrelation function was obtained with after pulsing suppression by means of fluorescence lifetime correlation spectroscopy with a pulsed 485-nM laser (40 mHz) in SymPhoTime (PicoQuant).

### Mammalian cell culture and immunofluorescence

NIH 3T3 fibroblasts (ATCC) were cultured in DMEM media and supplemented with 10% FBS, 2 mM L-glutamine, and penicillin-streptomycin. Cells were plated on glass coverslips for 24 h before fixation. Cells treated with latrunculin A (Sigma-Aldrich) were incubated with the drug at 1 µM for 15 min before fixation. Cells were fixed with 4% paraformaldehyde for 15 min, washed 3× in PBS, and then incubated for 10 min with 5 µg/ml Alexa Fluor 647 conjugated wheat germ agglutinin (Invitrogen) to label the membrane. Cells were washed 3× in PBS, permeabilized with 0.5% Triton X-100, and then incubated with Alexa Fluor 488 conjugated phalloidin (Invitrogen) and a rabbit anti–human Septin 7 primary antibody (IBL-America), followed by a goat anti–rabbit Alexa Fluor 567 (Invitrogen) secondary antibody. Coverslips were mounted on glass slides in ProLong Gold mounting media (Invitrogen).

Cells were imaged on an inverted Nikon Ti-E microscope with a Yokogawa CSU-X spinning disk scanhead, a laser merge module containing 491, 561, and 642 laser lines (Spectral Applied Research), and an HQ2 CoolSNAP CCD camera (Roper Scientific). Metamorph acquisition software (Molecular Devices) was used to control the microscope hardware. Images were acquired with a Nikon 60× 1.49 NA ApoTIRF oil-immersion objective.

### Online supplemental material

Tables S1, S2, and S3 list the fungal strains, plasmids, and oligos used in this study, respectively. Fig. S1 contains additional images of septins in *A. gossypii* and *S. cerevisiae*. Fig. S2 contains a graphical description of curvature and a visual example of curvature analysis in *A. gossypii*. Fig. S3 contains Coomassie-stained gels of septin purifications, characterization of the Cdc11-α6 mutant and a model of septin complex flexibility. Videos 1 and 2 demonstrate septin dynamics in *A. gossypii* and in vitro on supported lipid bilayer–coated beads, respectively. The following scripts are also included in the supplemental materials: filamentOrientation.m: Calculates filament angles with respect to branch angle; XT_MJG_MSJ_Curvature.m: Imaris XTension to calculate curvature values on an Imaris Surface and select curvature values within an ROI; and XT_ROI_part2_MSJ.m: Imaris XTension that complements XT_MJG_MSJ_Curvature.m by expediting the ROI selection process. Online supplemental material is available at http://www.jcb.org/cgi/content/full/jcb.201512029/DC1.


## Acknowledgments

We thank J. Moseley, H. Higgs, R. Sloboda, and A. Goryachev for critical reading of the manuscript; the Gladfelter Laboratory and R. Fischer for useful discussions; A. Lavanway for support with microscopes; K. Cottingham for statistical advice; M. Gastinger for help with curvature analysis; and J. Thorner, M. Mavrakis, and E. Spiliotis for sharing reagents.

This work was supported by grants from the National Science Foundation (MCB-507511 to A.S. Gladfelter) and the National Institutes of Health (NIGMS-T32GM008704 to A.A. Bridges).

The authors declare no competing financial interests.

Submitted: 7 December 2015
Accepted: 23 February 2016


## References


Bertin, A., M.A. McMurray, P. Grob, S.S. Park, G. Garcia III, I. Patanwala, H.L. Ng, T. Alber, J. Thorner, and E. Nogales. 2008. Saccharomyces cerevisiae septins: supramolecular organization of heterooligomers and the mechanism of filament assembly. *Proc. Natl. Acad. Sci. USA.* 105:8274–8279. http://dx.doi.org/10.1073/pnas.0803330105

Booth, E.A., E.W. Vane, D. Dovala, and J. Thorner. 2015. A Foerster Resonance Energy Transfer (FRET)-based System Provides Insight into the Ordered Assembly of Yeast Septin Hetero-octamers. *J. Biol. Chem.* 290:28388–28401. http://dx.doi.org/10.1074/jbc.M115.683128

Bowen, J.R., D. Hwang, X. Bai, D. Roy, and E.T. Spiliotis. 2011. Septin GTPases spatially guide microtubule organization and plus end dynamics in polarizing epithelia. *J. Cell Biol.* 194:187–197. http://dx.doi.org/10.1083/jcb.201102076

Bridges, A.A., and A.S. Gladfelter. 2015. Septin Form and Function at the Cell Cortex. *J. Biol. Chem.* 290:17173–17180. http://dx.doi.org/10.1074/jbc.R114.634444

Bridges, A.A., H. Zhang, S.B. Mehta, P. Occhipinti, T. Tani, and A.S. Gladfelter. 2014. Septin assemblies form by diffusion-driven annealing on membranes. *Proc. Natl. Acad. Sci. USA.* 111:2146–2151. http://dx.doi.org/10.1073/pnas.1314138111

Chao, J.T., A.K. Wong, S. Tavassoli, B.P. Young, A. Chruscicki, N.N. Fang, L.J. Howe, T. Mayor, L.J. Foster, and C.J. Loewen. 2014. Polarization of the endoplasmic reticulum by ER-septin tethering. *Cell.* 158:620–632. http://dx.doi.org/10.1016/j.cell.2014.06.033

DeMay, B.S., R.A. Meseroll, P. Occhipinti, and A.S. Gladfelter. 2009. Regulation of distinct septin rings in a single cell by Elm1p and Gin4p kinases. *Mol. Biol. Cell.* 20:2311–2326. http://dx.doi.org/10.1091/mbc.E08-12-1169

Dietrich, F.S., S. Voegeli, S. Brachat, A. Lerch, K. Gates, S. Steiner, C. Mohr, R. Pöhlmann, P. Luedi, S. Choi, et al. 2004. The Ashbya gossypii genome as a tool for mapping the ancient Saccharomyces cerevisiae genome. *Science.* 304:304–307. http://dx.doi.org/10.1126/science.1095781

Dinno, A. 2015. dunn.test: Dunn's Test of Multiple Comparisons Using Rank Sums. R package version 1.3.2. https://CRAN.R-project.org/package=dunn.test (accessed November 1, 2015).

Dolat, L., Q. Hu, and E.T. Spiliotis. 2014. Septin functions in organ system physiology and pathology. *Biol. Chem.* 395:123–141. http://dx.doi.org/10.1515/hsz-2013-0233

Elliott, H., R.S. Fischer, K.A. Myers, R.A. Desai, L. Gao, C.S. Chen, R.S. Adelstein, C.M. Waterman, and G. Danuser. 2015. Myosin II controls cellular branching morphogenesis and migration in three dimensions by minimizing cell-surface curvature. *Nat. Cell Biol.* 17:137–147. http://dx.doi.org/10.1038/ncb3092

Fares, H., M. Peifer, and J.R. Pringle. 1995. Localization and possible functions of Drosophila septins. *Mol. Biol. Cell.* 6:1843–1859. http://dx.doi.org/10.1091/mbc.6.12.1843

Fox, J., and S. Weisberg. 2011. An R Companion to Applied Regression. Sage, Thousand Oaks, CA. 472 pp.

Gilden, J., and M.F. Krummel. 2010. Control of cortical rigidity by the cytoskeleton: emerging roles for septins. *Cytoskeleton (Hoboken).* 67:477–486.

Gilden, J.K., S. Peck, Y.C. Chen, and M.F. Krummel. 2012. The septin cytoskeleton facilitates membrane retraction during motility and blebbing. *J. Cell Biol.* 196:103–114. http://dx.doi.org/10.1083/jcb.201105127

Gladfelter, A.S., L. Kozubowski, T.R. Zyla, and D.J. Lew. 2005. Interplay between septin organization, cell cycle and cell shape in yeast. *J. Cell Sci.* 118:1617–1628. http://dx.doi.org/10.1242/jcs.02286

Helfer, H., and A.S. Gladfelter. 2006. AgSwe1p regulates mitosis in response to morphogenesis and nutrients in multinucleated Ashbya gossypii cells. *Mol. Biol. Cell.* 17:4494–4512. http://dx.doi.org/10.1091/mbc.E06-03-0215

Hu, Q., L. Milenkovic, H. Jin, M.P. Scott, M.V. Nachury, E.T. Spiliotis, and W.J. Nelson. 2010. A septin diffusion barrier at the base of the primary cilium maintains ciliary membrane protein distribution. *Science.* 329:436–439. http://dx.doi.org/10.1126/science.1191054

Kinoshita, M., C.M. Field, M.L. Coughlin, A.F. Straight, and T.J. Mitchison. 2002. Self- and actin-templated assembly of Mammalian septins. *Dev. Cell.* 3:791–802. http://dx.doi.org/10.1016/S1534-5807(02)00366-0

Kroon, D.-J. 2009. Patch Normals. MATLAB Central File Exchange. http://www.mathworks.com/matlabcentral/fileexchange/24330-patch-normals (accessed March 22, 2016).

Kroon, D.-J. 2014. Patch Curvature. MATLAB Central File Exchange. http://www.mathworks.com/matlabcentral/fileexchange/32573-patch-curvature (accessed March 22, 2016).

Lisovich, A., and R. Day. 2014. rChoiceDialogs: rChoiceDialogs collection. R package version 1.0.6. https://CRAN.R-project.org/package=rChoiceDialogs (accessed November 1, 2015).

Longtine, M.S., C.L. Theesfeld, J.N. McMillan, E. Weaver, J.R. Pringle, and D.J. Lew. 2000. Septin-dependent assembly of a cell cycle-regulatory module in Saccharomyces cerevisiae. *Mol. Cell. Biol.* 20:4049–4061. http://dx.doi.org/10.1128/MCB.20.11.4049-4061.2000

Mavrakis, M., Y. Azou-Gros, F.C. Tsai, J. Alvarado, A. Bertin, F. Iv, A. Kress, S. Brasselet, G.H. Koenderink, and T. Lecuit. 2014. Septins promote F-actin ring formation by crosslinking actin filaments into curved bundles. *Nat. Cell Biol.* 16:322–334. http://dx.doi.org/10.1038/ncb2921

Mostowy, S., and P. Cossart. 2012. Septins: the fourth component of the cytoskeleton. *Nat. Rev. Mol. Cell Biol.* 13:183–194.

Mostowy, S., S. Janel, C. Forestier, C. Roduit, S. Kasas, J. Pizarro-Cerdá, P. Cossart, and F. Lafont. 2011. A role for septins in the interaction between the Listeria monocytogenes INVASION PROTEIN InlB and the Met receptor. *Biophys. J.* 100:1949–1959. http://dx.doi.org/10.1016/j.bpj.2011.02.040

Ramamurthi, K.S., S. Lecuyer, H.A. Stone, and R. Losick. 2009. Geometric cue for protein localization in a bacterium. *Science.* 323:1354–1357. http://dx.doi.org/10.1126/science.1169218

Sirajuddin, M., M. Farkasovsky, F. Hauer, D. Kühlmann, I.G. Macara, M. Weyand, H. Stark, and A. Wittinghofer. 2007. Structural insight into filament formation by mammalian septins. *Nature.* 449:311–315. http://dx.doi.org/10.1038/nature06052

Tada, T., A. Simonetta, M. Batterton, M. Kinoshita, D. Edbauer, and M. Sheng. 2007. Role of Septin cytoskeleton in spine morphogenesis and dendrite development in neurons. *Curr. Biol.* 17:1752–1758. http://dx.doi.org/10.1016/j.cub.2007.09.039

Tanaka-Takiguchi, Y., M. Kinoshita, and K. Takiguchi. 2009. Septin-mediated uniform bracing of phospholipid membranes. *Curr. Biol.* 19:140–145. http://dx.doi.org/10.1016/j.cub.2008.12.030

Tooley, A.J., J. Gilden, J. Jacobelli, P. Beemiller, W.S. Trimble, M. Kinoshita, and M.F. Krummel. 2009. Amoeboid T lymphocytes require the septin cytoskeleton for cortical integrity and persistent motility. *Nat. Cell Biol.* 11:17–26. http://dx.doi.org/10.1038/ncb1808

Warnes, G.R., B. Bolker, G. Gorjanc, G. Grothendieck, A. Korosec, T. Lumley, D. MacQueen, A. Magnusson, J. Rogers, et al. 2015a. gdata: Various R Programming Tools for Data Manipulation. R package version 2.17.0. https://cran.r-project.org/package=gdata (accessed November 1, 2015).

Warnes, G.R., B. Bolker, and T. Lumley. 2015b. gtools: Various R Programming Tools. R package version 3.5.0. https://CRAN.R-project.org/package=gtools (accessed November 1, 2015).

Wickham, H. 2007. Reshaping Data with the reshape Package. *J. Stat. Softw.* 21:1–20. http://dx.doi.org/10.18637/jss.v021.i12

Wickham, H. 2009. ggplot2: elegant graphics for data analysis. Springer, New York. 213 pp.

Wickham, H., and R. Francois. 2015. dplyr: A Grammar of Data Manipulation. R package version 0.4.3. https://CRAN.Rproject.org/package=dplyr (accessed November 1, 2015).

Winston, C. 2014. extrafont: Tools for using fonts. R package version 0.17. https://CRAN.R-project.org/package=extrafont (accessed November 1, 2015).

Xie, Y., J.P. Vessey, A. Konecna, R. Dahm, P. Macchi, and M.A. Kiebler. 2007. The GTP-binding protein Septin 7 is critical for dendrite branching and dendritic-spine morphology. *Curr. Biol.* 17:1746–1751. http://dx.doi.org/10.1016/j.cub.2007.08.042

Zimmerberg, J., and M.M. Kozlov. 2006. How proteins produce cellular membrane curvature. *Nat. Rev. Mol. Cell Biol.* 7:9–19. http://dx.doi.org/10.1038/nrm1784